Journal of Applied Physics

Changes in band alignment during annealing at 600 °C of ALD Al_2O_3 on $(In_xGa_{1-x})_2O_3$ for x = 0.25–0.74

Cite as: J. Appl. Phys. **127**, 105701 (2020); https://doi.org/10.1063/5.0002875
Submitted: 28 January 2020 . Accepted: 21 February 2020 . Published Online: 09 March 2020

Chaker Fares, Minghan Xian, David J. Smith, Martha R. McCartney, Max Kneiß, Holger von Wenckstern, Marius Grundmann, Marko Tadjer, Fan Ren, and S. J. Pearton

© 2020 Author(s).

Journal of Applied Physics ARTICLE scitation.org/journal/jap

Changes in band alignment during annealing at 600 °C of ALD Al_2O_3 on $(In_xGa_{1-x})_2O_3$ for $x = 0.25–0.74$

Cite as: J. Appl. Phys. **127**, 105701 (2020); doi: 10.1063/5.0002875
Submitted: 28 January 2020 · Accepted: 21 February 2020 ·
Published Online: 9 March 2020

Chaker Fares,[1] Minghan Xian,[1] David J. Smith,[2] Martha R. McCartney,[2] Max Kneiß,[3] Holger von Wenckstern,[3] Marius Grundmann,[3] Marko Tadjer,[4] Fan Ren,[1] and S. J. Pearton[5,a)]

AFFILIATIONS

[1]Department of Chemical Engineering, University of Florida, Gainesville, Florida 32611, USA
[2]Department of Physics, Arizona State University, Tempe, Arizona 85287, USA
[3]Universität Leipzig, Felix-Bloch-Institut für Festkörperphysik, 04103 Leipzig, Germany
[4]U.S. Naval Research Laboratory, Washington, DC 20375, USA
[5]Department of Materials Science and Engineering, University of Florida, Gainesville, Florida 32611, USA

[a)]**Author to whom correspondence should be addressed:** spear@mse.ufl.edu

ABSTRACT

Changes in valence band offsets (VBOs) as a result of annealing of heterostructures of atomic layer deposited Al_2O_3 on $(In_xGa_{1-x})_2O_3$ (where $x = 0.25–0.75$), grown by pulsed laser deposition, are reported. The heterostructures have been annealed at 600 °C to simulate the expected thermal budget during device fabrication. The VBOs decrease significantly as a result of annealing, with the change being larger at higher indium concentrations. The decrease in VBO ranges from −0.38 eV for $(In_{0.25}Ga_{0.75})_2O_3$ to −1.28 eV for $(In_{0.74}Ga_{0.26})_2O_3$ and is likely due to increased interfacial disorder at the heterointerface as well as phase differences between gallium-rich samples and indium-rich samples. After annealing, the band alignment remains type I (nested gap) for x = 0.25, 42, and 60 but becomes type II for the $(In_{0.74}Ga_{0.26})_2O_3$ sample.

Published under license by AIP Publishing. https://doi.org/10.1063/5.0002875

I. INTRODUCTION

As Ga_2O_3-based technologies develop, there is growing interest in alloying Ga_2O_3 with In_2O_3 to tune the wavelength response of photodetectors and increase the mobility in heterostructure transistors.[1–6] In order for such $(In_xGa_{1-x})_2O_3$ based structures to be realized, studies have focused on the behavior of charge accumulation layers, miscibility gaps, and native defect behavior as monoclinic Ga_2O_3 is alloyed with cubic In_2O_3.[1–5,7–22] To date, several groups have reviewed the phase stability and the crystal structure of $(In_xGa_{1-x})_2O_3$, which can show four, five, or sixfold coordinated cation sites.[1,2] A number of methods to fabricate $(In_xGa_{1-x})_2O_3$ have been reported including sputtering, sol-gel processing, organic chemical vapor deposition, pulsed laser deposition (PLD), and molecular beam epitaxy, with each method yielding different phase stabilities.[1,3,5,6,8,12,19,21,23–32]

An important aspect for any application of $(In_xGa_{1-x})_2O_3$ is the band alignment with dielectrics commonly used for surface passivation or metal–oxide–semiconductor (MOS) gates on transistors. To mitigate leakage current in MOS-based devices, valence and conduction band offsets should ideally be larger than 1 eV.[33,34] One of the most common dielectrics for these applications is Al_2O_3 due to its dielectric constant, large bandgap, and well-established deposition conditions. Al_2O_3 can be deposited using many methods; however, atomic layer deposition (ALD) is desirable because it is a well-controlled, conformal, and low-damage process.[35]

$(In_xGa_{1-x})_2O_3$ based devices may face several scenarios where high temperatures are encountered. To fabricate MOS-based transistors utilizing Ga_2O_3, it is necessary to anneal devices at temperatures between 500 and 600 °C for Ohmic contact formation or after ion implantation for device isolation.[36–39] Additionally, due to low thermal conductivity of Ga_2O_3, junction temperatures can rise

Published under license by AIP Publishing.

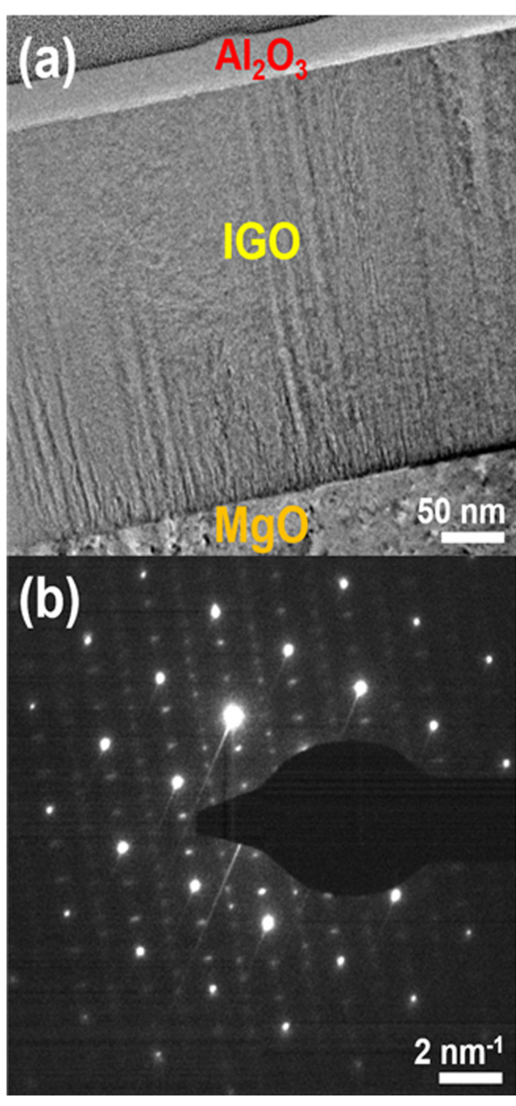

FIG. 1. (a) Cross section TEM image and (b) selected-area electron diffraction pattern (SAED) from gallium-rich portion of the $(In_xGa_{1-x})_2O_3$ wafer.

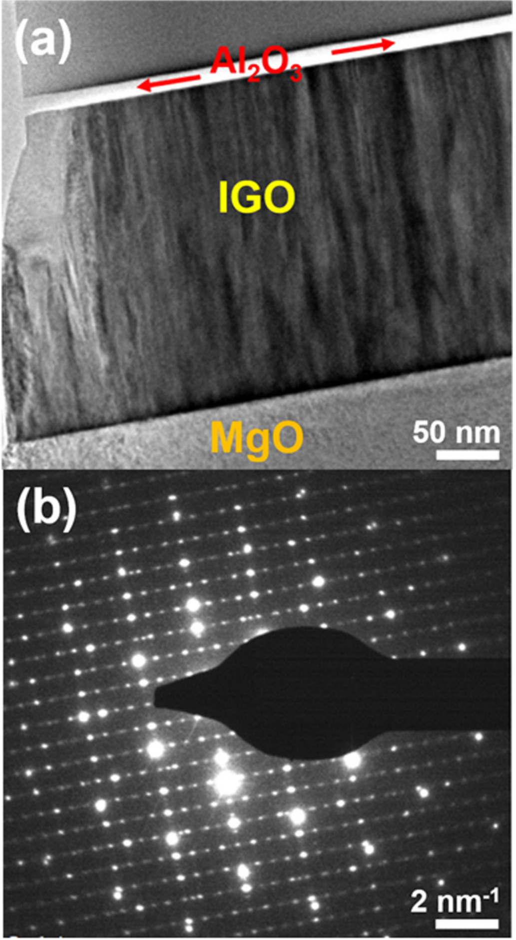

FIG. 2. (a) Cross section TEM image and (b) selected-area electron diffraction pattern (SAED) from indium-rich portion of the $(In_xGa_{1-x})_2O_3$ wafer.

significantly under high-current application.[40–42] Thus far, there have been no reports on how high temperatures affect the band offset between Al_2O_3 and $(In_xGa_{1-x})_2O_3$. Zhou *et al.*[43] reported that lower interface state densities were achieved after 500 °C annealing of ALD Al_2O_3 on Ga_2O_3, but no band alignment studies were performed. In this report, we describe the effects of post-deposition annealing at 600 °C on the band alignment of atomic layer deposited Al_2O_3 on $(In_xGa_{1-x})_2O_3$.

II. EXPERIMENTAL

$(In_xGa_{1-x})_2O_3$ thin films were grown on 2-in. MgO (0001) substrates using continuous-composition-spread Pulsed Laser Deposition (CCS-PLD) and segmented targets of In_2O_3 and Ga_2O_3.[1,2,26,28,29,44–46] The growth temperature for these samples was 650 °C and the oxygen pressure was 0.08 mbar. Along the length of the wafer, the In concentration varied between 16% and 86%. The increase in In concentration had an S-shaped profile along the gradient of the wafer, in agreement with theoretical calculations.[47] Energy-dispersive x-ray spectroscopy (EDX) was used to verify the spatial grading of the chemical composition.[2,47] Perpendicular to the gradient direction, the In concentration was constant. The (111)-oriented cubic bixbyite phase was dominant for the In-rich portion of the wafer, while the monoclinic phase was dominant for Ga-rich compositions.[19] After growth of $(In_xGa_{1-x})_2O_3$ films, the wafer was diced in order to study specific film compositions. The compositions for this study were $x = 0.25$, 0.42, 0.60, and 0.74, determined using x-ray Photoemission Spectroscopy (XPS) and verified using the growth map generated via EDX. Alignment marks were utilized to mark exact positions on each sample for measurement. The uncertainty in the spatial

Published under license by AIP Publishing.

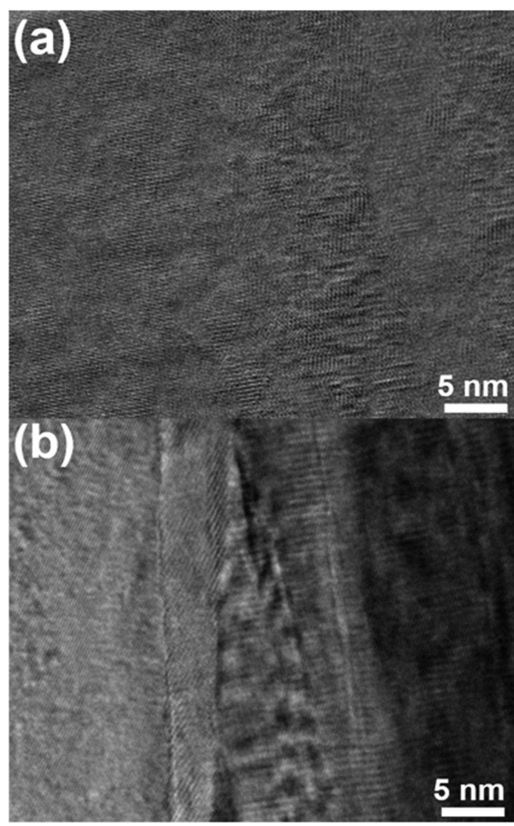

FIG. 3. High-resolution TEM images showing the upper part of (a) gallium-rich portion of the $(In_xGa_{1-x})_2O_3$ wafer and (b) indium-rich portion of the $(In_xGa_{1-x})_2O_3$ wafer.

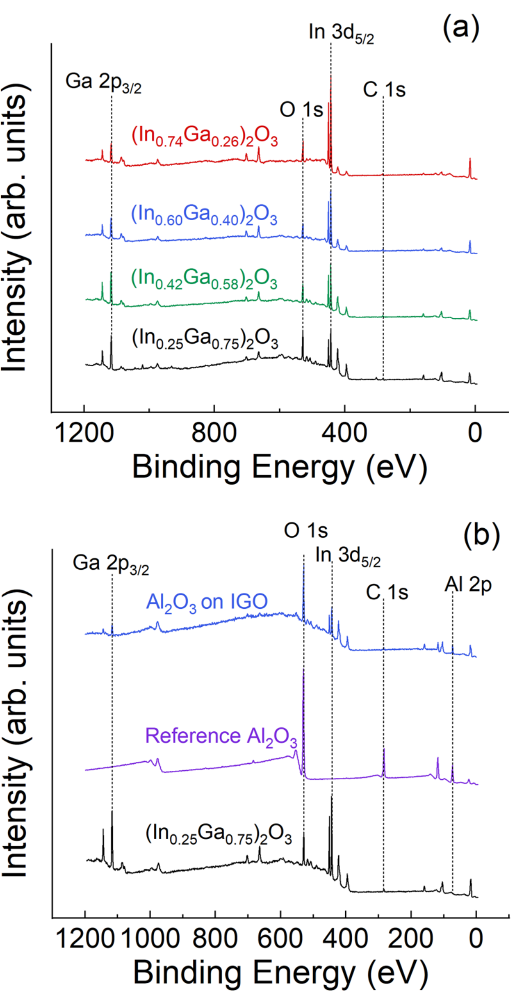

FIG. 4. XPS survey scans: (a) $(In_xGa_{1-x})_2O_3$ for aluminum concentrations studied, and (b) thick ALD SiO_2 and its heterostructure on IGO. The intensity is in arbitrary units (a.u.).

correlation after dicing was less than 50 μm, which corresponded to a potential compositional variation of ±2% for all samples. The measured bandgaps of each sample were 4.55 eV for $(In_{0.25}Ga_{0.75})_2O_3$, 4.35 eV for $(In_{0.42}Ga_{0.58})_2O_3$, 4.2 eV for $(In_{0.60}Ga_{0.40})_2O_3$, and 4.05 eV for $(In_{0.74}Ga_{0.26})_2O_3$, as described in more detail in a previous report.[48]

Before atomic layer deposition of Al_2O_3, the samples were cleaned using acetone and isopropyl alcohol rinses, followed by N_2 drying and ozone exposure for 15 min. After cleaning, the samples were loaded into the ALD system within a cleanroom environment. Thick (200 nm) films of Al_2O_3 were deposited to measure the dielectric core levels and bandgap. Thin (1.5 nm) layers of Al_2O_3 for measuring the electronic structure of the $Al_2O_3/(In_xGa_{1-x})_2O_3$ heterostructure were deposited in a Cambridge Nano Fiji 200 using a remote plasma mode. The deposition temperature of Al_2O_3 was 200 °C. The precursors were trimethylaluminum and a 300-W inductively coupled plasma (ICP) to generate atomic oxygen.[49,50]

Sections from the samples were annealed at 600 °C under N_2 ambient for 30 s in a rapid thermal annealing system. The valence band offsets (VBOs) were measured in both as-deposited and annealed samples. This temperature was chosen since it is at the high end of Ohmic contact alloying conditions, as well as tuning of the resistance in implant isolation regions for inter-device isolation. Thus, it represents a realistic test of interface stability during the thermal budget encountered during device processing.

The XPS system was a Physical Instruments ULVAC PHI, with a monochromatic Al x-ray source (source power 300 W, energy 1486.6 eV), a takeoff angle of 50°, an acceptance angle of 7°, and an analysis area of 100 μm in diameter. The electron pass energy was 93.5 eV for survey scans and 23.5 eV for high-resolution scans. The XPS survey scans were used to ensure that Al_2O_3, $(In_xGa_{1-x})_2O_3$, and heterostructures of the two were free from contamination and impurities.[51] The energy resolution of the XPS system is approximately 0.5 eV, and binding energy accuracy is within 0.03 eV.

An ion beam and a simultaneous electron flood gun were utilized to avoid sample charging. In addition, the samples were

Published under license by AIP Publishing.

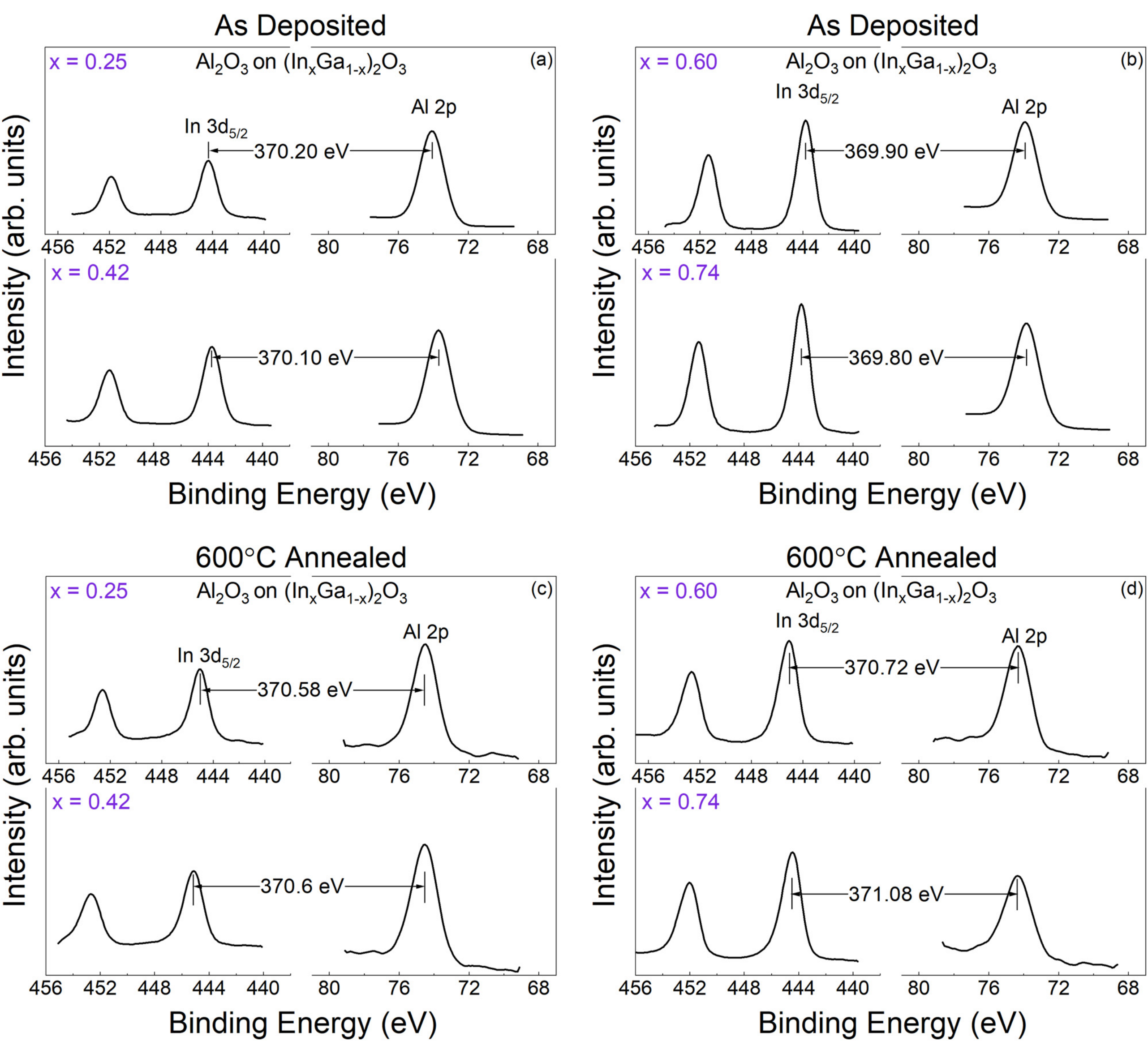

FIG. 5. High-resolution XPS spectra: (a) and (b) $(In_xGa_{1-x})_2O_3$ to Al_2O_3 core delta regions as-deposited and (c) and (d) after annealing at 600 °C for 5 min in N_2 ambient. The intensity is in arbitrary units (a.u.).

insulated electronically from the platen to prevent uneven charge dispersion from the sample to the chuck. The C 1s core level of adventitious carbon (284.8 eV) was used to calibrate the binding energy on all samples. The valence band offset was determined using only relative energy positions so the absolute energy calibration had no effect on the final offset. By using the flood gun, differential charging was not observed during XPS data collection. The bandgap of ALD-deposited Al_2O_3 was measured using Reflection Electron Energy Loss Spectroscopy (REELS) utilizing a 1 kV electron beam and hemispherical analyzer.

An aberration-corrected FEI Titan 80-300 electron microscope operated at 300 kV was used to record TEM images of the $(In_xGa_{1-x})_2O_3$ films. Samples were prepared for cross-sectional observation using an FEI Nova 200 focused-ion-beam system.

III. RESULTS AND DISCUSSION

Transmission electron microscopy was used to investigate the microstructure of $(In_xGa_{1-x})_2O_3$ wafers. Figure 1 shows a TEM image and the corresponding selected-area electron diffraction

Published under license by AIP Publishing.

pattern (SAED) from the Ga-rich portion [$(In_{0.25}Ga_{0.75})_2O_3$] of the $(In_xGa_{1-x})_2O_3$ wafer. The IGO sample is crystalline in nature and epitaxial with the MgO substrate, with no major crystallographic defects such as grain boundaries and threading dislocations. Figure 2 shows a TEM image and the corresponding SAED pattern from the indium-rich portion of the $(In_xGa_{1-x})_2O_3$ wafer, $(In_{0.74}Ga_{0.26})_2O_3$. The film is again crystalline and epitaxial, but it also contains columnar grains extending through the film, with typical widths in the range of 5–20 nm. Figure 3 shows high-resolution TEM images taken from (a) the Ga-rich portion of the $(In_xGa_{1-x})_2O_3$ wafer and (b) the In-rich portion of the $(In_xGa_{1-x})_2O_3$ wafer. The Ga-rich portion is relatively homogeneous across the field of view, whereas the In-rich portion contains grain boundaries and also shows some possible phase separation. Thus, there are notable crystallographic and structural differences between gallium-rich and indium-rich portions of the wafer, as also shown in previous XRD studies.[19,29] For the compositions examined here, two main phases are present, namely, the monoclinic phase of β-Ga_2O_3 and the cubic phase of bixbyite In_2O_3. For higher indium compositions, the rhombohedral $InGaO_3$ (II) phase was also observed. Due to the presence of these separate phases, a direct correlation between the lattice constants and In content is not possible for these samples.

Figure 4 shows XPS survey scans from (a) $(In_xGa_{1-x})_2O_3$ concentrations from $(In_{0.25}Ga_{0.75})_2O_3$ to $(In_{0.74}Ga_{0.26})_2O_3$ and (b) thick ALD Al_2O_3 and its heterostructure on IGO. As shown in the survey scans, no contamination was present for any of the samples and only lattice constituents are present. Reflection Electron Energy Loss Spectroscopy (REELS) on the thick ALD Al_2O_3 sample yielded a bandgap of 6.9 eV that is similar to previous reports.[52,53]

Figures 5(a) and 5(b) show high-resolution XPS scans for $(In_xGa_{1-x})_2O_3$ to Al_2O_3 core delta regions in the as-deposited condition. After taking these measurements, the heterostructure samples along with the reference $(In_xGa_{1-x})_2O_3$ and bulk Al_2O_3 were annealed at 600 °C for 5 min in N_2 ambient. Figures 5(c) and 5(d) show high-resolution XPS scans of same heterostructure core delta regions after annealing. Table I lists the peak locations prior to and after annealing. There was no change in the peak location and valence band maximum (VBM) for the reference $(In_xGa_{1-x})_2O_3$ and bulk Al_2O_3 after annealing. The VBMs for $(In_xGa_{1-x})_2O_3$ samples were 2.5 ± 0.15 eV for $(In_{0.25}Ga_{0.76})_2O_3$, 2.25 ± 0.15 eV for $(In_{0.42}Ga_{0.58})_2O_3$, 2.25 ± 0.15 eV for $(In_{0.60}Ga_{0.40})_2O_3$, and 2.10 ± 0.15 eV for $(In_{0.74}Ga_{0.26})_2O_3$. A root-sum-square relationship combining the error bars in different binding energies was then used to determine the potential deviation in the overall valence band (VB) offset. Using VBM values, core level locations, and measured bandgaps of each sample, the VB offset and corresponding conduction band (CB) offset could then be calculated.[51,54,55] The VB offsets for the as-deposited Al_2O_3 on $(In_xGa_{1-x})_2O_3$ were 0.88 ± 0.20 eV for $(In_{0.25}Ga_{0.76})_2O_3$, 0.98 ± 0.20 eV for $(In_{0.42}Ga_{0.58})_2O_3$, 1.13 ± 0.25 eV for $(In_{0.60}Ga_{0.40})_2O_3$, and 1.23 ± 0.25 eV for $(In_{0.74}Ga_{0.26})_2O_3$. After annealing, these offsets changed significantly.

Figure 6 illustrates the measured change in VB offsets for the annealed $Al_2O_3/(In_xGa_{1-x})_2O_3$ heterostructures and their values prior to annealing. Across all compositions studied, the annealing process caused a significant decrease in the VB offset. As the In concentration was increased, the shift in VB offset also

TABLE I. Summary of the measured reference and heterostructure peaks for Al_2O_3 on $(In_xGa_{1-x})_2O_3$ (eV) before and after annealing at 600 °C for 5 min in N_2 ambient.

Indium concentration	Reference $(In_xGa_{1-x})_2O_3$			Reference Al_2O_3			Thin Al_2O_3 on $(In_xGa_{1-x})_2O_3$: As deposited		Thin Al_2O_3 on $(In_xGa_{1-x})_2O_3$: Annealed at 600 °C	
	Core level peak (In $3d_{5/2}$)	VBM	Core–VBM	Core level peak (Al 2p)	VBM	Core–VBM	Δ core level (In $3d_{5/2}$ − Al 2p)	Valence band offset	Δ core level	VBO
$(In_{0.25}Ga_{0.75})_2O_3$	444.65	2.50	442.15	74.32	3.25	71.07	370.2	0.88	370.58	0.5
$(In_{0.42}Ga_{0.58})_2O_3$	444.40	2.25	442.15	⋮	⋮	⋮	370.1	0.98	370.6	0.48
$(In_{0.60}Ga_{0.40})_2O_3$	444.35	2.25	442.10	⋮	⋮	⋮	369.9	1.13	370.72	0.31
$(In_{0.74}Ga_{0.26})_2O_3$	444.20	2.10	442.10	⋮	⋮	⋮	369.8	1.23	371.08	−0.05

Published under license by AIP Publishing.

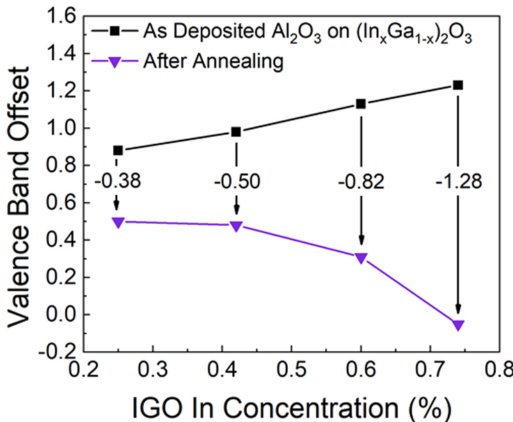

FIG. 6. Valence band offsets for as-deposited and annealed Al_2O_3/$(In_xGa_{1-x})_2O_3$ heterostructures as a function of indium concentration.

increased. The cause is likely to be changes in interfacial chemistry. Figure 7 shows cross-sectional images before and after annealing. After annealing, the In-rich end does not show any obvious change in morphology and crystallinity, yet it has the largest change in VB measurements. Conversely, Ga-rich samples show less change in the VB alignment yet exhibit a more pronounced morphology change within $(In_xGa_{1-x})_2O_3$. This change is minimal to non-existent near the MgO growth substrate and becomes more pronounced in the IGO further away from the MgO growth substrate. A potential cause of this post-annealing crystallinity change is that In_2O_3 is thermodynamically less stable than Ga_2O_3, with Gibbs energies of formation of −198.6 kcal/mol and −238.6 kcal/mol for In_2O_3 and Ga_2O_3, respectively.[56,57] Additionally, In–O bonds break more easily than Ga–O, based on their diatomic bond strengths. Using this information, the change in band alignment in the indium-rich sample could be larger due to the relative instability of In compared to Ga within the structure. Despite gallium-rich samples showing significant crystallinity changes within the bulk IGO, the interfacial chemistry dominates the band alignments as determined by the surface-sensitive XPS.

Figure 8 shows band diagrams for Al_2O_3/$(In_xGa_{1-x})_2O_3$ heterostructures: (a) as-deposited and (b) after annealing at 600 °C for

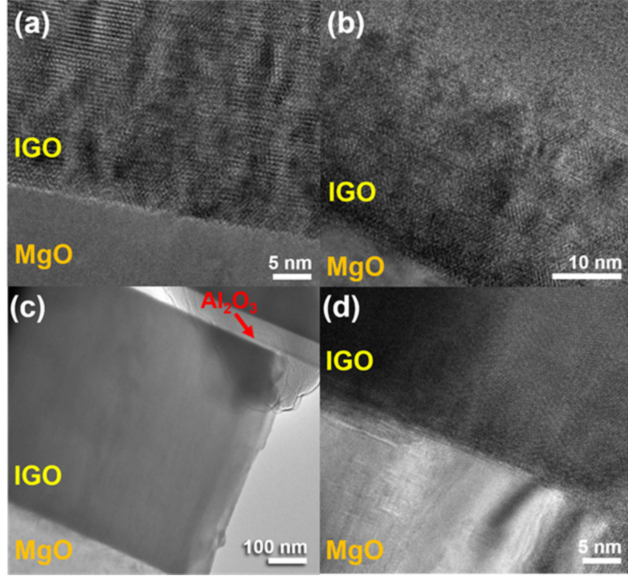

FIG. 7. Cross section TEM images of (a) the substrate-epi region of a Ga-rich sample prior to annealing, (b) the same region after annealing, (c) an In-rich sample after annealing, and (d) the magnified image of the same region.

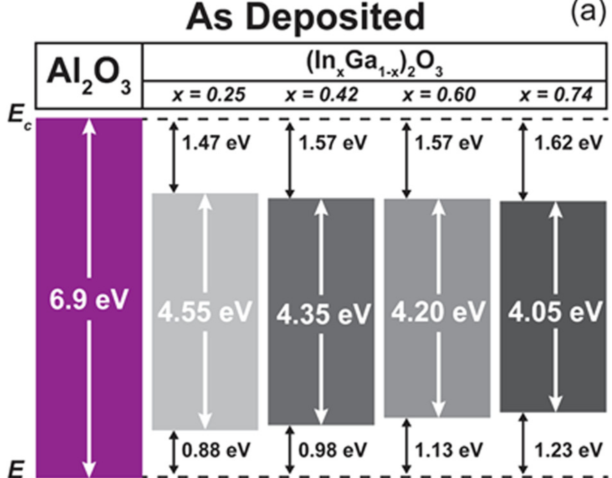

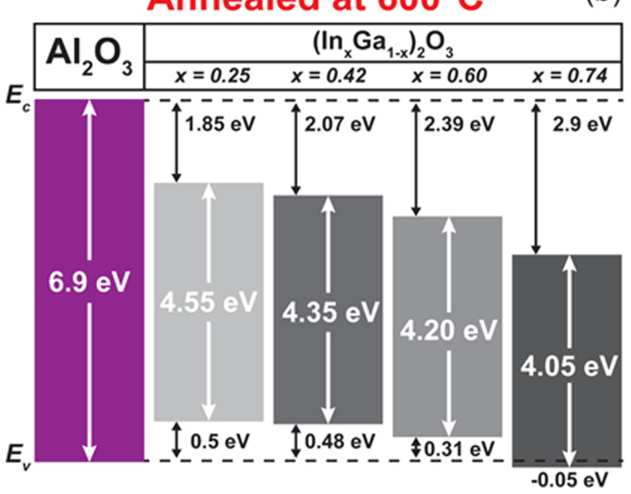

FIG. 8. Band diagrams for Al_2O_3/$(In_xGa_{1-x})_2O_3$ heterostructure: (a) as deposited and (b) after annealing at 600 °C for 5 min in N_2 ambient.

Published under license by AIP Publishing.

5 min in N_2 ambient. For the as-deposited heterostructure, Al_2O_3 yields adequate offsets in both conduction and valence bands, allowing for good carrier confinement for all compositions of $(In_xGa_{1-x})_2O_3$. As shown in Fig. 8(b), annealing significantly shifted the band alignment. The VB offsets were reduced for all compositions studied, while the reduction was most pronounced for high-indium concentration samples. The band alignment is type I for x = 0.25 to x = 0.6 and shifts to type II for the x = 0.74 sample. Hole confinement is marginal for all heterostructures after annealing.

IV. SUMMARY AND CONCLUSION

The effects of post-deposition annealing on the band alignment of $Al_2O_3/(In_xGa_{1-x})_2O_3$ heterostructures were measured over a range of In concentrations (x = 0.25–0.74). Prior to annealing, the band alignment is type I across this composition range. The valence band offset was reduced after annealing at 600 °C, with the change being larger for higher In concentrations. The changes in valence band offset were determined more by interfacial chemistry than by visible crystalline disorder after annealing. The band alignment remains type I (nested gap) for x = 0.25, 42, and 60 but becomes type II for the $(In_{0.74}Ga_{0.26})_2O_3$ sample after annealing. In future, additional work should be done on interface state densities after annealing, radiation effects on band alignment, and dielectric engineering to fabricate high-k dielectrics that also have bandgaps wide enough to be used with Ga_2O_3-based devices and their alloyed derivatives.

ACKNOWLEDGMENTS

This work was supported by the Department of the Defense, Defense Threat Reduction Agency, under No. HDTRA1-17-1-011, monitored by Jacob Calkins and also by the National Science Foundation (No. DMR 1856662; Tania Paskova). Research at Naval Research Laboratory was supported by the Office of Naval Research (ONR), partially under Award No. N00014-15-1-2392. The authors at Leipzig thank Jörg Lenzner for EDX measurements and Monika Hahn for PLD target preparation. D.J.S. and M.R.M. acknowledge use of facilities in the John M. Cowley Center for High Resolution Electron Microscopy at Arizona State University. M.K. acknowledges support by the European Social Fund within the Young Investigator Group "Oxide Heterostructures" (No. SAB 100310460) and the Leipzig School for Natural Sciences BuildMoNa.

DATA AVAILABILITY

The data that support the findings of this study are available from the corresponding author upon reasonable request.

REFERENCES

[1]H. von Wenckstern, Adv. Electron. Mater. **3**, 1600350 (2017).
[2]H. von Wenckstern, *Gallium Oxide* (Elsevier, 2019), pp. 119–148.
[3]F. Zhang, H. Li, M. Arita, and Q. Guo, Opt. Mater. Express **7**, 3769 (2017).
[4]Z. Zhang, H. Von Wenckstern, J. Lenzner, M. Lorenz, and M. Grundmann, Appl. Phys. Lett. **108**, 123503 (2016).
[5]Y. Kokubun, T. Abe, and S. Nakagomi, Phys. Status Solidi A **207**, 1741–1745 (2010).
[6]F. Zhang, K. Saito, T. Tanaka, M. Nishio, and Q. Guo, Solid State Commun. **186**, 28–31 (2014).
[7]R. Schmidt-Grund, C. Kranert, T. Böntgen, H. Von Wenckstern, H. Krauß, and M. Grundmann, J. Appl. Phys. **116**, 053510 (2014).
[8]D. D. Edwards, P. E. Folkins, and T. O. Mason, J. Am. Ceram. Soc. **80**, 253–257 (1997).
[9]V. Wang, W. Xiao, D. M. Ma, R. J. Liu, and C. M. Yang, J. Appl. Phys. **115**, 043708 (2014).
[10]M. B. Maccioni and V. Fiorentini, Appl. Phys. Express **9**, 041102 (2016).
[11]H. Peelaers, D. Steiauf, J. B. Varley, A. Janotti, and C. G. Van De Walle, Phys. Rev. B Condens. Matter Mater. Phys. **92**, 085206 (2015).
[12]X. Wang, Z. Chen, K. Saito, T. Tanaka, M. Nishio, and Q. Guo, J. Alloys Compd. **690**, 287–292 (2017).
[13]P. D. C. King, T. D. Veal, D. J. Payne, A. Bourlange, R. G. Egdell, and C. F. McConville, Phys. Rev. Lett. **101**, 116808 (2008).
[14]F. Yang, J. Ma, C. Luan, and L. Kong, Appl. Surf. Sci. **255**, 4401–4404 (2009).
[15]M. Baldini, M. Albrecht, D. Gogova, R. Schewski, and G. Wagner, Semicond. Sci. Technol. **30**, 024013 (2015).
[16]P. Vogt and O. Bierwagen, APL Mater. **4**, 086112 (2016).
[17]T. Oshima and S. Fujita, Phys. Status Solidi **5**, 3113–3115 (2008).
[18]F. Fuchs and F. Bechstedt, Phys. Rev. B Condens. Matter Mater. Phys. **77**, 155107 (2008).
[19]C. Kranert, J. Lenzner, M. Jenderka, M. Lorenz, H. Von Wenckstern, R. Schmidt-Grund, and M. Grundmann, J. Appl. Phys. **116**, 013505 (2014).
[20]G. Patzke and M. Binnewies, Solid State Sci. **2**, 689–699 (2000).
[21]J. M. Phillips, J. Kwo, G. A. Thomas, S. A. Carter, R. J. Cava, S. Y. Hou, J. J. Krajewski, J. H. Marshall, W. F. Peck, D. H. Rapkine, and R. B. Van Dover, Appl. Phys. Lett. **65**, 115–117 (1994).
[22]C. Janowitz, V. Scherer, M. Mohamed, A. Krapf, H. Dwelk, R. Manzke, Z. Galazka, R. Uecker, K. Irmscher, R. Fornari, M. Michling, D. Schmeißer, J. R. Weber, J. B. Varley, and C. G. Van De Walle, New J. Phys. **13**, 085014 (2011).
[23]M. Grundmann, H. Frenzel, A. Lajn, M. Lorenz, F. Schein, and H. von Wenckstern, Phys. Status Solidi A **207**, 1437–1449 (2010).
[24]W. T. Lin, C. Y. Ho, Y. M. Wang, K. H. Wu, and W. Y. Chou, J. Phys. Chem. Solids **73**, 948–952 (2012).
[25]F. Zhang, K. Saito, T. Tanaka, M. Nishio, and Q. Guo, J. Alloys Compd. **614**, 173–176 (2014).
[26]M. Kneiß, P. Storm, G. Benndorf, M. Grundmann, and H. von Wenckstern, ACS Comb. Sci. **20**, 643–652 (2018).
[27]H. Von Wenckstern, Z. Zhang, F. Schmidt, J. Lenzner, H. Hochmuth, and M. Grundmann, CrystEngComm. **15**, 10020–10027 (2013).
[28]H. von Wenckstern, D. Splith, A. Werner, S. Müller, M. Lorenz, and M. Grundmann, ACS Comb. Sci. **17**, 710–715 (2015).
[29]H. Von Wenckstern, D. Splith, M. Purfürst, Z. Zhang, C. Kranert, S. Müller, M. Lorenz, and M. Grundmann, Semicond. Sci. Technol. **30**, 024005 (2015).
[30]D. C. Hays, B. P. Gila, S. J. Pearton, and F. Ren, Appl. Phys. Rev. **4**, 021301 (2017).
[31]T. Minami, Y. Takeda, T. Kakumu, S. Takata, and I. Fukuda, J. Vac. Sci. Technol. A **15**, 958–962 (1997).
[32]A. Wang, N. L. Edleman, J. R. Babcock, T. J. Marks, M. A. Lane, P. R. Brazis, and C. R. Kannewurf, J. Mater. Res. **17**, 3155–3162 (2002).
[33]Z. Feng, Q. Feng, J. Zhang, C. Zhang, H. Zhou, X. Li, L. Huang, L. Xu, Y. Hu, S. Zhao, and Y. Hao, J. Alloys Compd. **745**, 292–298 (2018).
[34]C. Fares, F. Ren, E. Lambers, D. C. Hays, B. P. Gila, and S. J. Pearton, J. Vac. Sci. Technol. B **36**, 061207 (2018).
[35]C. Fares, F. Ren, D. C. Hays, B. P. Gila, and S. J. Pearton, ECS J. Solid State Sci. Technol. **8**, Q3001–Q3006 (2019).
[36]S. J. Pearton, J. Yang, P. H. Cary, F. Ren, J. Kim, M. J. Tadjer, and M. A. Mastro, Appl. Phys. Rev. **5**, 011301 (2018).
[37]N. A. Moser, J. P. McCandless, A. Crespo, K. D. Leedy, A. J. Green, E. R. Heller, K. D. Chabak, N. Peixoto, and G. H. Jessen, Appl. Phys. Lett. **110**, 143505 (2017).

Published under license by AIP Publishing.

[38]A. J. Green, K. D. Chabak, M. Baldini, N. Moser, R. Gilbert, R. C. Fitch, G. Wagner, Z. Galazka, J. Mccandless, A. Crespo, K. Leedy, and G. H. Jessen, IEEE Electron Device Lett. **38**, 790–793 (2017).
[39]C. Joishi, Y. Zhang, Z. Xia, W. Sun, A. R. Arehart, S. Ringel, S. Lodha, and S. Rajan, IEEE Electron Device Lett. **40**, 1241–1244 (2019).
[40]J. Yang, M. Xian, P. Carey, C. Fares, J. Partain, F. Ren, M. Tadjer, E. Anber, D. Foley, A. Lang, J. Hart, J. Nathaniel, M. L. Taheri, S. J. Pearton, and A. Kuramata, Appl. Phys. Lett. **114**, 232106 (2019).
[41]M. Xian, C. Fares, F. Ren, B. P. Gila, Y.-T. Chen, Y.-T. Liao, M. Tadjer, and S. J. Pearton, J. Vac. Sci. Technol. B **37**, 061201 (2019).
[42]M. Xian, R. Elhassani, C. Fares, F. Ren, M. Tadjer, and S. J. Pearton, J. Vac. Sci. Technol. B **37**, 061205 (2019).
[43]H. Zhou, S. Alghamdi, M. Si, G. Qiu, and P. D. Ye, IEEE Electron Device Lett. **37**, 1411–1414 (2016).
[44]A. Hassa, H. Von Wenckstern, D. Splith, C. Sturm, M. Kneiß, V. Prozheeva, and M. Grundmann, APL Mater. **7**, 022525 (2019).
[45]M. Kneiß, A. Hassa, D. Splith, C. Sturm, H. Von Wenckstern, T. Schultz, N. Koch, M. Lorenz, and M. Grundmann, APL Mater. **7**, 101102 (2019).
[46]M. Lorenz, H. Hochmuth, C. Grüner, H. Hilmer, A. Lajn, D. Spemann, M. Brandt, J. Zippel, R. Schmidt-Grund, H. Von Wenckstern, and M. Grundmann, Laser Chem. **2010**, 140976 (2010).
[47]H. von Wenckstern, Z. Zhang, F. Schmidt, J. Lenzner, H. Hochmuth, and M. Grundmann, CrystEngComm. **15**, 10020 (2013).
[48]C. Fares, M. Kneiß, H. von Wenckstern, M. Grundmann, M. Tadjer, F. Ren, E. Lambers, and S. J. Pearton, APL Mater. **7**, 071115 (2019).
[49]C. Fares, F. Ren, E. Lambers, D. C. Hays, B. P. Gila, and S. J. Pearton, J. Electron. Mater. **48**, 1568–1573 (2019).
[50]C. Fares, F. Ren, E. Lambers, D. C. Hays, B. P. Gila, and S. J. Pearton, Semicond. Sci. Technol. **34**, 025006 (2019).
[51]E. A. Kraut, R. W. Grant, J. R. Waldrop, and S. P. Kowalczyk, Phys. Rev. Lett. **44**, 1620–1623 (1980).
[52]C. Fares, M. Kneiß, H. von Wenckstern, M. Tadjer, F. Ren, E. Lambers, M. Grundmann, and S. J. Pearton, ECS J. Solid State Sci. Technol. **8**, P351–P356 (2019).
[53]C. Fares, M. Kneiss, H. von Wenckstern, M. Grundmann, M. J. Tadjer, F. Ren, D. Hays, B. P. Gila, and S. J. Pearton, ECS Trans. **92**, 79–88 (2019).
[54]M. Perego and G. Seguini, J. Appl. Phys. **110**, 053711 (2011).
[55]M. T. Nichols, W. Li, D. Pei, G. A. Antonelli, Q. Lin, S. Banna, Y. Nishi, and J. L. Shohet, J. Appl. Phys. **115**, 094105 (2014).
[56]E. Martinez, H. Grampeix, O. Desplats, A. Herrera-Gomez, O. Ceballos-Sanchez, J. Guerrero, K. Yckache, and F. Martin, Chem. Phys. Lett. **539–540**, 139 (2012).
[57]X. Feng, Z. Li, W. Mi, and J. Ma, Vacuum **124**, 101 (2016).

Published under license by AIP Publishing.